ARTICLES
https://doi.org/10.1038/s41567-020-01062-6

nature physics

Check for updates

Electrically tunable correlated and topological states in twisted monolayer–bilayer graphene

Shaowen Chen[1,2,8], Minhao He[3,8], Ya-Hui Zhang[4], Valerie Hsieh[1], Zaiyao Fei[3], K. Watanabe[5], T. Taniguchi[6], David H. Cobden[3], Xiaodong Xu[3,7] ✉, Cory R. Dean[1] ✉ and Matthew Yankowitz[3,7] ✉

Twisted van der Waals heterostructures with flat electronic bands have recently emerged as a platform for realizing correlated and topological states with a high degree of control and tunability. In graphene-based moiré heterostructures, the correlated phase diagram and band topology depend on the number of graphene layers and the details of the external environment from the encapsulating crystals. Here, we report that the system of twisted monolayer–bilayer graphene (tMBG) hosts a variety of correlated metallic and insulating states, as well as topological magnetic states. Because of its low symmetry, the phase diagram of tMBG approximates that of twisted bilayer graphene when an applied perpendicular electric field points from the bilayer towards the monolayer graphene, or twisted double bilayer graphene when the field is reversed. In the former case, we observe correlated states that undergo an orbitally driven insulating transition above a critical perpendicular magnetic field. In the latter case, we observe the emergence of electrically tunable ferromagnetism at one-quarter filling of the conduction band, and an associated anomalous Hall effect. The direction of the magnetization can be switched by electrostatic doping at zero magnetic field. Our results establish tMBG as a tunable platform for investigating correlated and topological states.

In select van der Waals (vdW) heterostructures, coupling to a moiré superlattice renormalizes the band structure and results in nearly flat electronic bands. These systems act as highly tunable platforms capable of hosting a variety of correlated and topological ground states, including correlated insulating (CI) states, superconductivity and ferromagnetism with an associated quantum anomalous Hall effect (QAHE)[1–21]. In moiré heterostructures composed entirely of graphene, the correlated phase diagram depends sensitively on the number of graphene sheets. In twisted bilayer graphene (tBLG)—two rotated sheets of monolayer graphene—CI states and superconductivity can be induced and tuned by changing the twist angle[1–5,8,9] and by applying pressure[3]. In addition, ferromagnetism and a QAHE can be obtained in the system by further rotationally aligning tBLG with a boron nitride (BN) substrate[6,7]. In twisted double bilayer graphene (tDBG)—two rotated sheets of Bernal-stacked bilayer graphene—spin-polarized CI states are observed that can be further tuned by application of a perpendicular electric field[11–15]. Finally, three layers of rhombohedrally stacked graphene rotationally aligned with BN can also manifest CI states and ferromagnetism with non-trivial band topology[16–18].

Heterostructures comprising rotated sheets of monolayer and Bernal-stacked bilayer graphene have so far not been investigated experimentally, but are theoretically promising candidates to host correlated and topological states because of their flat electronic bands with non-zero Chern numbers[22–24]. Twisted monolayer–bilayer graphene (tMBG) has low crystal symmetry, breaking both two-fold rotation, C_2, and mirror reflection, M_y. The former exchanges opposite valleys within the same layer, and the latter exchanges the top and bottom components of the twisted heterostructure (Fig. 1a). Consequentially, these states are anticipated to be uniquely tunable with a simple combination of a single twist angle θ, gate doping n and perpendicular displacement field D, without any additional complicating conditions involving an internal crystal stacking configuration[16–18] or coupling to a secondary moiré pattern[6,7].

Here, we investigate electrical transport in dual-gated tMBG devices over a small range of twist angles, $0.89° < \theta < 1.55°$ (see Fig. 1 and Extended Data Figs. 1 and 2). We find that the correlated phase diagram of tMBG can approximately resemble either tBLG or tDBG depending on the direction of D. When D points from the bilayer towards the monolayer graphene, we observe correlated states at all integer filling factors similar to tBLG, with the exception that superconductivity does not occur. Although correlations appear to be weaker than in tBLG, CI states emerge above a critical perpendicular magnetic field. When the direction of the electric field is flipped, we observe a spin-polarized CI state at half filling of the conduction band, similar to tDBG. tMBG also exhibits correlated magnetic states with intrinsic topological order in this configuration, which can be controlled by the twist angle, electric field and doping. Our work thus provides a means of realizing a wide array of tunable correlated and topological states within a single material platform.

Figure 1b shows the continuum model calculation of the band structure of tMBG at a twist angle of $\theta = 1.08°$ as a function of the interlayer potential difference, δ (Methods). In contrast to tBLG and tDBG, the low symmetry of tMBG means that the band structure differs depending on the direction of D (meaning the sign of δ). Additionally, calculations of the layer-resolved local density of states (LDOS) reveal that it is favourable for charge to be arranged

---

[1]Department of Physics, Columbia University, New York, NY, USA. [2]Department of Applied Physics and Applied Mathematics, Columbia University, New York, NY, USA. [3]Department of Physics, University of Washington, Seattle, WA, USA. [4]Department of Physics, Harvard University, Cambridge, MA, USA. [5]Research Center for Functional Materials, National Institute for Materials Science, Tsukuba, Japan. [6]International Center for Materials Nanoarchitectonics, National Institute for Materials Science, Tsukuba, Japan. [7]Department of Materials Science and Engineering, University of Washington, Seattle, WA, USA. [8]These authors contributed equally: Shaowen Chen, Minhao He. ✉e-mail: xuxd@uw.edu; cd2478@columbia.edu; myank@uw.edu

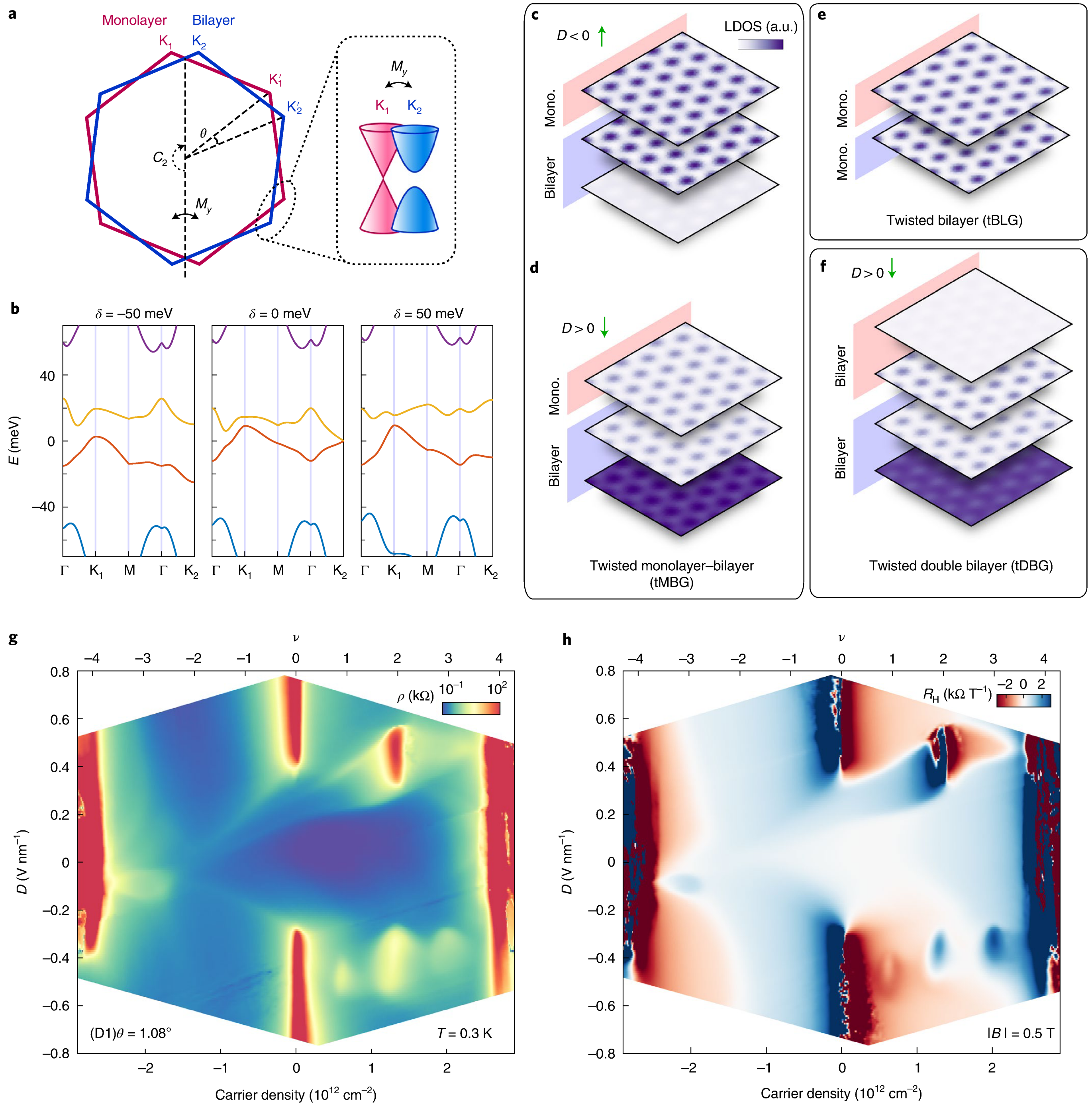

Fig. 1 | Electronic structure of tMBG and transport in a device with $\theta = 1.08°$. **a**, First Brillouin zones of monolayer (red) and bilayer (blue) graphene, rotated by a twist angle θ. Both C_2 rotation symmetry and M_y mirror symmetry are broken in tMBG. **b**, Calculated band structures of tMBG with $\theta = 1.08°$ at various values of interlayer potential, δ. **c**–**f**, Corresponding calculated local density of states for each layer of tMBG at full filling of the conduction band with $D < 0$ (**c**) and $D > 0$ (**d**). Green arrows indicate the direction of the electric field. They are compared with the local density of states (LDOS) calculated for tBLG (**e**) and tDBG (**f**) at the same twist angle. The rotated interface is between layers with different colour projections (red or blue). **g**, Resistivity of device D1 at $T = 0.3$ K. The corresponding band filling factor ν is shown on the top axis. **h**, Corresponding Hall coefficient, R_H, antisymmetrized at $|B| = 0.5$ T.

highly asymmetrically among the three constituent graphene layers. Figure 1c,d shows the LDOS of tMBG calculated at full filling of the conduction band for opposite signs of D. In both cases, the moiré potential localizes the LDOS on a triangular lattice of ABB-stacked sites (analogous to AA-stacked sites in tBLG, in which the carbon atoms sit directly atop one another). For $D < 0$ ($\delta < 0$), when the field points from the bilayer towards the monolayer graphene, the LDOS on the outer sheet of the bilayer graphene is suppressed, and the LDOS on the two graphene layers at the rotated interface resembles that of tBLG (Fig. 1e). On the other hand, for $D > 0$ ($\delta > 0$), the LDOS on the outer graphene layer is instead enhanced. In this case the LDOS resembles that of tDBG (Fig. 1f), where the fourth (uppermost) graphene layer has a small LDOS. We would therefore anticipate that tMBG will act similarly to either tBLG or tDBG

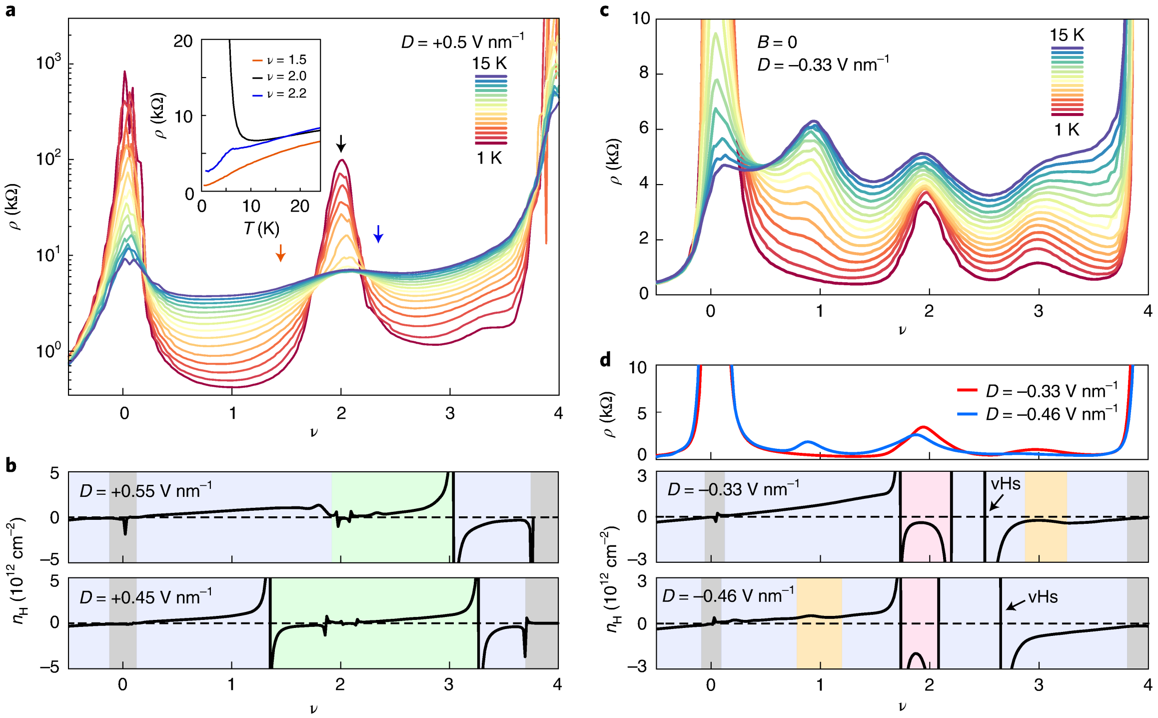

Fig. 2 | Transport characteristics of correlated states in tMBG. a, Temperature dependence of ρ at $D = +0.5\,\mathrm{V\,nm^{-1}}$. Inset: $\rho(T)$ acquired at the filling factors denoted by the coloured arrows in the main panel. **b**, Hall density, n_H, as a function of ν at various D. Colour shading denotes regions of the phase diagram with different inferred degeneracy, where blue corresponds to four-fold degeneracy and green corresponds to two-fold degeneracy. Grey-shaded regions denote insulating states at $\nu = 0$ and 4. **c**, Temperature dependence of ρ at $D = -0.33\,\mathrm{V\,nm^{-1}}$. **d**, Top: ρ versus ν at selected D and $T = 0.3\,\mathrm{K}$. Bottom: corresponding n_H. Colour shading is as in **b**, but with pink denoting regions with correlation-driven sign changes in n_H and gold denoting regions with deviations from the anticipated gate-induced density, n. An additional sign change related to the single-particle vHs is denoted by an arrow.

depending on the sign of D, assuming the additional or absent layer of lightly doped graphene plays a limited role.

This picture is borne out by the experiments. Figure 1g shows the resistivity ρ of a tMBG device with $\theta = 1.08°$ (device D1) as a function of carrier density n and D at temperature $T = 0.3\,\mathrm{K}$. The top axis indicates the filling factor of the bands, ν (Methods). Qualitatively, many of the observed features can be associated with the band structure calculated in Fig. 1b (Extended Data Fig. 3). In particular, at $\nu = 0$ the device behaves as a semi-metal for small $|D|$, but becomes semiconducting at larger $|D|$. Insulating features are observed over a wide range of $|D|$ at full filling of the conduction or valence band ($\nu = \pm 4$). Additional resistance peaks disperse as a function of D within the flat bands, and probably correspond to van Hove singularities (vHs) as in tDBG[15].

In the conduction band ($0 < \nu < +4$), additional resistive peaks are observed over a finite range of D that appear to have no counterparts in the single-particle model. These resistive peaks are observed at integer ν, each within a different finite range of D. Notably, these features are inequivalent for opposite signs of D, in contrast to tBLG and tDBG, where the correlated states are approximately symmetric with D. Measurements of the antisymmetrized Hall coefficient, $R_H = (R_{xy}[B] - R_{xy}[-B])/(2B)$, provide additional insight into their nature (Fig. 1h). For $D > 0$, there is a highly resistive state at half filling surrounded by a stretched halo of somewhat increased resistance. As in tDBG, R_H changes sign within this extended halo region, suggestive of a spontaneously broken symmetry within the bands[15]. By contrast, for $D < 0$ there are three weakly resistive features at each integer ν, and abrupt changes in R_H occur only near these features.

Figure 2a shows the temperature dependence of ρ in the conduction band at $D = +0.5\,\mathrm{V\,nm^{-1}}$, in which we expect the LDOS distribution to resemble that of tDBG. We observe clear insulating behaviour at half filling ($\nu = 2$), with energy gaps that appear to grow on applying an in-plane magnetic field indicative of spin-polarized ordering (Extended Data Fig. 4). Slightly away from half filling, we observe abrupt drops in ρ as the temperature is lowered (blue curve, inset, Fig. 2a). These abrupt drops arise within regions of the phase diagram in which the magnitude or sign of the Hall density, $n_H \equiv 1/eR_H$, departs from single-particle expectations (green shaded regions, Fig. 2b). This behaviour has been observed previously in comparable regions of the tDBG phase diagram and is understood to probably arise as a consequence of the development of symmetry-broken correlated metallic states within the flat conduction band[15]. Overall, our observations correspond closely with the behaviour of the CI and metallic states in tDBG[11–15], suggesting that at this twist angle the phase diagram of tMBG is similar to that of tDBG, with small differences arising due to the absence of the weakly charged fourth graphene sheet (Fig. 1f).

Figure 2c shows a similar temperature dependence of ρ at $D = -0.33\,\mathrm{V\,nm^{-1}}$, at which we expect the LDOS distribution to resemble that of tBLG. The states at $\nu = 1, 2, 3$ all exhibit metallic temperature dependence, defined by a reduction in ρ as T is lowered, in direct contrast to the behaviour of the CI state for $D > 0$. Notably, the feature at $\nu = 1$ is apparent at high temperature ($T = 15\,\mathrm{K}$ in Fig. 2c), but becomes suppressed at low temperature. Qualitatively similar behaviour has been observed previously in tBLG, most clearly in devices with twist angles slightly detuned from the 'magic angle'[3] and in devices with strong electrostatic screening from a nearby metal gate[9]. This suggests that our devices are marginally correlated compared to magic angle tBLG, potentially due to a combination of larger bandwidth (Extended Data Fig. 3) and electrostatic screening from the addition of the weakly charged third graphene sheet. However, unlike in tBLG, these states can be tuned with D.

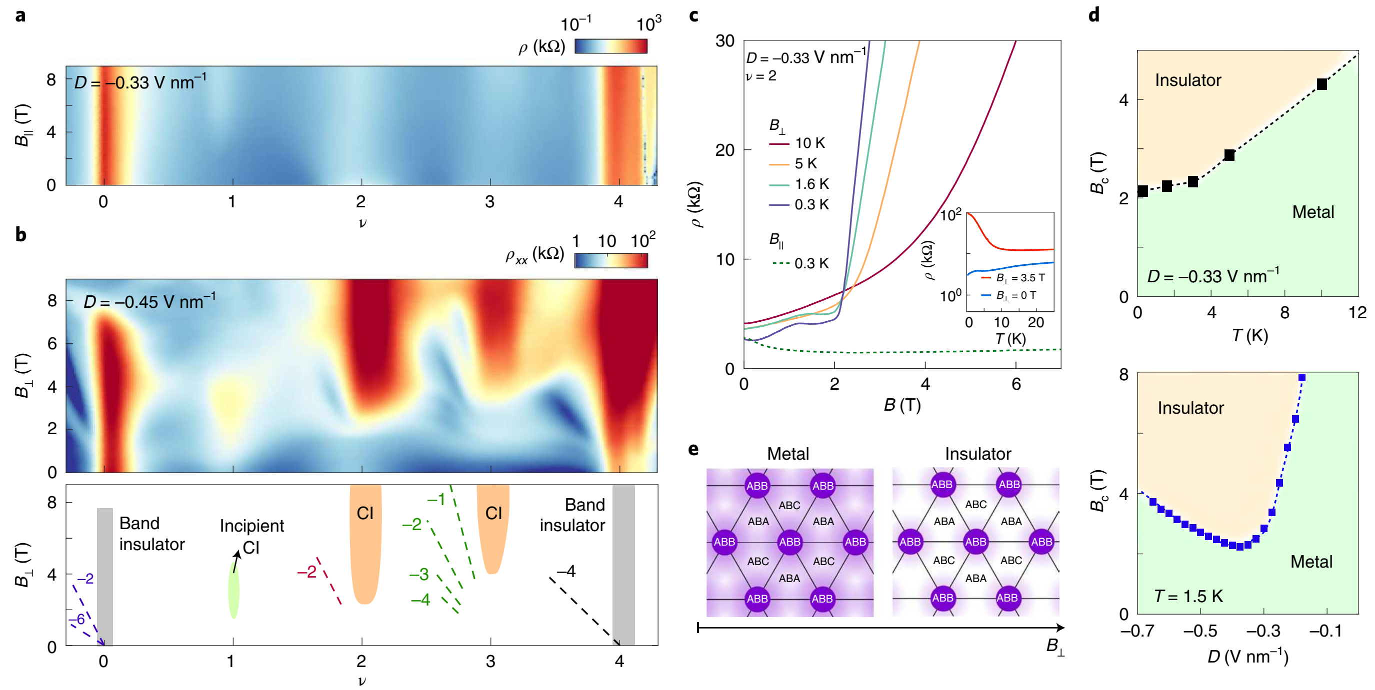

Fig. 3 | Properties of the correlated states at $\nu = 1, 2, 3$ for $D < 0$. **a**, Device resistivity up to full filling of the moiré unit cell with $D = -0.33$ V nm^{-1} as a function of $B_{\parallel}$ at $T = 300$ mK. **b**, Landau fan diagram with $D = -0.45$ V nm^{-1}. The bottom panel schematically denotes the observed quantum oscillations as well as the band insulator states (grey), CI states (orange) and an incipient CI state (green). CI states at $\nu = 2, 3$ and associated quantum oscillations only emerge for finite $B_{\perp}$. **c**, $\rho(B_{\perp})$ at various T (solid curves) and $\rho(B_{\parallel})$ at $T = 300$ mK. Inset: $\rho(T)$ at $\nu = 2$ for $B_{\perp} = 0$ and 3.5 T. **d**, Critical magnetic field for the onset of insulating behaviour, B_c, versus T (top) and D (bottom). Dashed lines are guides to the eye. Regions coloured green correspond to metallic temperature dependence, whereas beige regions correspond to insulating behaviour. **e**, Cartoon schematics of the inferred LDOS (light pink) on the moiré lattice (ABB sites are denoted by dark purple dots) as a function of $B_{\perp}$.

For example, Fig. 2d shows ρ for two values of D, in which the state at $\nu = 1$ is apparent at $D = -0.46$ V nm^{-1} but not at $D = -0.33$ V nm^{-1}. These correlated metallic states are also associated with anomalies in n_H (Fig. 2d): either a sign change (pink shading) or deviations from a linear gate-induced charge density n (gold shading). An additional sign change in n_H is observed for $2 < \nu < 3$ that matches the vHs in the single-particle band structure (Supplementary Fig. 1), suggesting that correlations do not greatly modify the conduction band Fermi surface at filling factors away from the integers.

The correlated metallic states observed for $D < 0$ have little to no dependence on magnetic field applied in plane, $B_{\parallel}$ (shown up to 9 T in Fig. 3a). However, applying a perpendicular field, $B_{\perp}$, causes a sharp transition to an insulating behaviour at $\nu = 2$ and 3 above a critical field value (Fig. 3b). Signs of an incipient resistive state can also be seen over a finite range of $B_{\perp}$ at $\nu = 1$. Quantum oscillations associated with the states at $\nu = 2$ and 3 emerge only above a finite $B_{\perp}$, with apparent two-fold degeneracy neighbouring $\nu = 2$ and no remaining degeneracies neighbouring $\nu = 3$ (Fig. 3b, lower panel). This is consistent with previous studies of tBLG[3,8,9], in which recent measurements have indicated that a Dirac-like dispersion is revived at each quarter band filling due to a cascade of spontaneously broken symmetries[25,26].

Figure 3c shows $\rho(B_{\perp})$ at $\nu = 2$ for various temperatures (solid curves), as well as $\rho(B_{\parallel})$ at $T = 0.3$ K (dashed curve). Although ρ is nearly insensitive to $B_{\parallel}$, we observe an abrupt transition to insulating behaviour above a critical perpendicular magnetic field, B_c, at each temperature, defined as the crossover point between separate linear fits to $\rho(B_{\parallel})$ at low and high $B_{\perp}$. The inset of Fig. 3c compares $\rho(T)$ at $B_{\perp} = 0$ and 3.5 T for $\nu = 2$, showing the metallic and insulating behaviour, respectively (Extended Data Fig. 5 for $\nu = 1$, 3). We find that B_c first grows weakly with increasing temperature, then increases rapidly at higher temperature (Fig. 3d). B_c can also be tuned with D, as shown for $T = 1.5$ K in Fig. 3d. It is peculiar that insulating behaviour onsets with $B_{\perp}$ but has almost no dependence on $B_{\parallel}$. In the simple approximation of a perfectly 2D sample, $B_{\perp}$ couples to both the spin and orbital Zeeman energies whereas $B_{\parallel}$ only couples to the spin Zeeman energy. Consequentially, spin-polarized (unpolarized) states are typically strengthened (suppressed) by a magnetic field pointing in either orientation. The correlated states for $D < 0$ do not appear to have a natural interpretation in this context.

Insulating states emerging with $B_{\perp}$ have been observed previously in bulk correlated systems including Bechgaard salts[27] and high-mobility semiconductors such as $Hg_{1-x}Cd_xTe$ (refs. [28,29]). These insulating states were thought to be driven by orbital confinement effects, associated with spin-density waves in the former and Wigner crystal formation in the latter. The overall similarity of our $B_c(T)$ to those results suggests that related orbital confinement effects may be at play in tMBG. Phenomenologically similar behaviour has also been observed in the $\nu = 0$ quantum Hall states of monolayer and bilayer graphene. The ground state is thought to be a spin antiferromagnet in the absence of explicit sublattice symmetry breaking[30], and originates from spontaneous valley anisotropy driven by orbital effects. Although these states should be stabilized at any finite $B_{\perp}$, disorder can result in an artificial high-field transition between a metallic and insulating state at $\nu = 0$ in graphene[31]. However, in disordered graphene the low-field resistance is independent of temperature, in contrast to our observations of metallic temperature dependence (Extended Data Fig. 5d). Therefore, it is more likely that the correlated states we observe here require a finite $B_{\perp}$ to undergo an orbitally driven transition from a metallic to an insulating ground state. Future experiments in a tilted magnetic

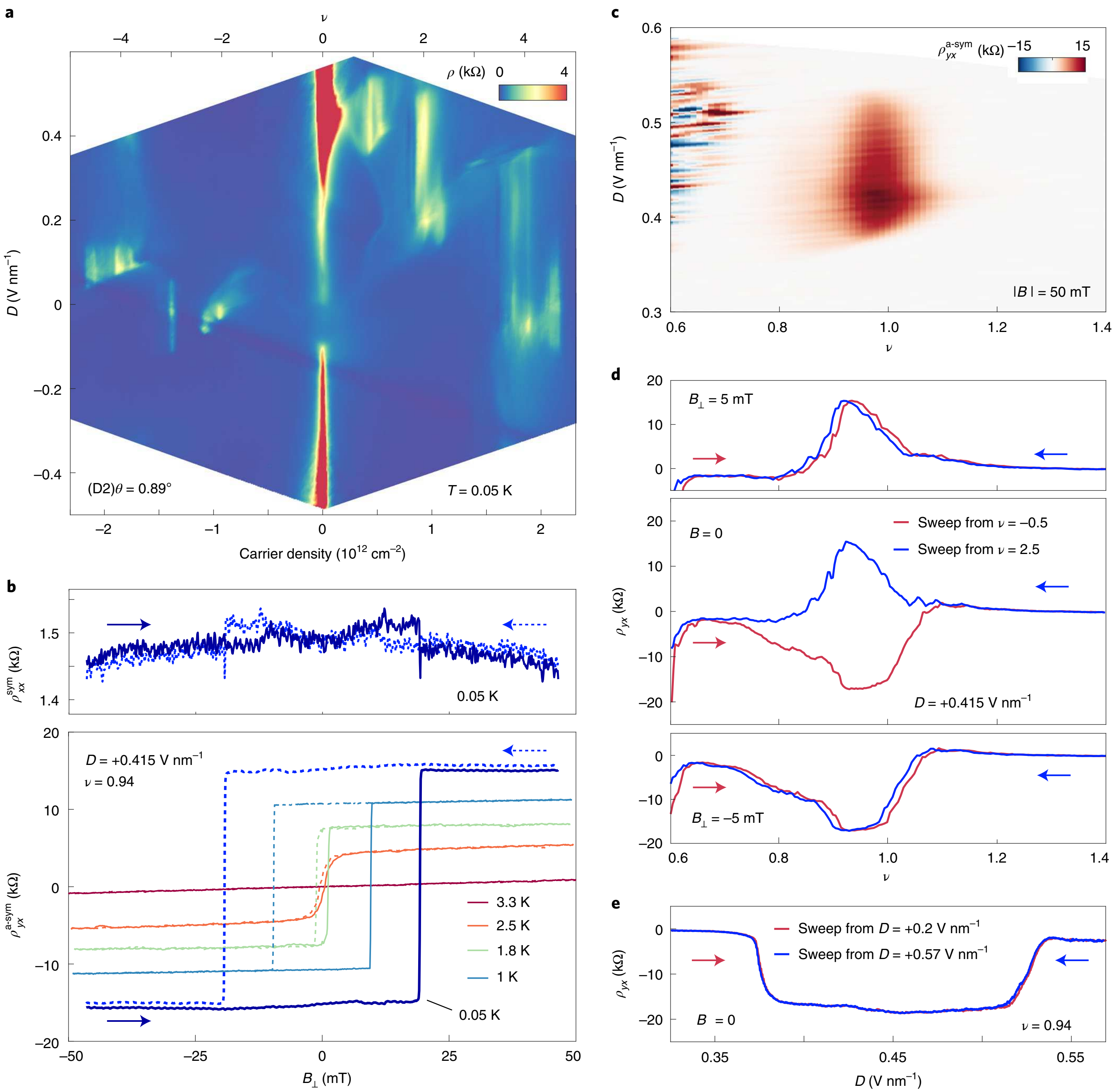

Fig. 4 | Ferromagnetism and AHE at $\nu = 1$ for $D > 0$ in a device with $\theta = 0.89°$. a, Resistivity of device D2 at $T = 0.05$ K. The corresponding band filling factor ν is shown on the top axis. **b**, Symmetrized ρ_{xx} and antisymmetrized ρ_{yx} acquired as $B_\perp$ is swept back and forth at $\nu = 0.94$ and $D = +0.415$ V nm^{-1} with $T = 0.05$ K (blue curves). ρ_{yx} is also shown at different temperatures. Arrows indicate the direction of the magnetic field sweep, corresponding to solid and dashed curves. **c**, ρ_{yx}, antisymmetrized at $|B| = 50$ mT. Rapidly oscillating red and blue points near $\nu \approx 0.6$ are related to the nearby insulating charge neutrality point rather than magnetic order. **d**, ρ_{yx} as ν is swept back and forth from −0.5 to +2.5, acquired at $B_\perp = 5$ mT, 0 and −5 mT (top to bottom). $B = 0$ corresponds to zero current in the superconducting magnet coil, with the offset due to trapped flux being less than ~1 mT. **e**, ρ_{yx} as D is swept back and forth from +0.2 V nm^{-1} to +0.57 V nm^{-1} at $B = 0$.

field should help to further elucidate the spin and valley ordering of these states.

The cartoon schematic in Fig. 3e qualitatively illustrates the presumed atomic-scale electronic structure of tMBG in the metallic and field-assisted insulating phases. The dark purple sites correspond to regions of ABB stacking, and the lighter pink halo represents the associated LDOS. $B_\perp$ is expected to orbitally confine the LDOS more tightly around the ABB sites, resulting in an enhancement in the effective interaction strength. By contrast, the LDOS does not depend strongly on $B_\parallel$, as orbital effects are anticipated to be weak due to the atomically thin nature of tMBG, and therefore the interaction strength is also not substantially modified. Although our results at $D < 0$ appear to share a number of qualitative similarities with weakly correlated tBLG, one important difference is that superconductivity appears to be absent in our device, whereas it remains a robust ground state even in screened tBLG devices[8,9,32].

Differences in bandwidth may be a contributing factor (Extended Data Fig. 3), but it is also possible that the low symmetry of tMBG plays a role. Superconductivity may be sensitive to the combination of C_2 (ref. [33]) and M_y symmetries, both broken in tMBG. So far there have been no unambiguous reports of superconductivity in a moiré vdW platform with broken C_2 symmetry[15].

Finally, we turn to the correlated states emerging for $D>0$ in a second device (device D2) with a slightly smaller twist angle, $\theta=0.89°$. Figure 4a shows the resistivity of device D2 at $T=0.05$ K and $B=0$ T. The overall behaviour is similar to device D1, with a few key exceptions. First, the insulating behaviour is weak or absent at $\nu=\pm4$, indicating the energy gaps to the remote bands are small or zero at this twist angle. Second, incipient CI states can be seen at $\nu=-2$ and -3 for $D\approx0$ (Supplementary Fig. 3) and have no known analogue in tDBG. Third, an additional resistive state emerges at $\nu=1$ over a small range of $D>0$. This state exhibits a robust anomalous Hall effect (AHE) with large Hall angle $\rho_{yx}/\rho_{xx}\approx10$ at $B=0$ (blue curves, Fig. 4b). ρ_{yx} exhibits hysteresis about zero magnetic field, an unambiguous characteristic of ferromagnetism. A single loop with a coercive field of $B_\perp\approx20$ mT is formed as the field is swept back and forth. We field symmetrize ρ_{xx} and antisymmetrize ρ_{yx} to eliminate small offsets in the two due to mixing (Supplementary Fig. 2). The temperature dependence of the ferromagnetism is also shown in Fig. 4b. The hysteresis and magnitude of the AHE are suppressed on raising the temperature and vanish above $T\approx2.5$ K (Extended Data Fig. 6). The sharpness of the magnetization flip implies that the easy axis is perpendicular to the sample, and that a single magnetic domain is dominant within the measured region of the sample.

Figure 4c shows a map of ρ_{yx} antisymmetrized at $|B|=50$ mT. The regime of ferromagnetic order as a function of ν and D is indicated by the dark red at $\nu\approx1$. The ferromagnetism occurs over an extended range of D, and persists into the metallic states slightly outside the $\nu=1$ gap. We do not observe any signs of ferromagnetic ordering at any other filling factors in this device. Despite the fact that ρ_{yx} is not quantized to an integer fraction of h/e^2, and ρ_{xx} does not vanish, the large Hall angle indicates transport through edge states. Nonlocal resistance measurements provide further evidence supporting chiral edge conduction in our sample (Supplementary Fig. 4)[6,34]. It seems likely that a fully developed Chern insulator state could be realized in a sample with lower disorder or a larger energy gap. In a model of the isolated conduction band of tMBG as four overlapping flat bands with varying spin and valley order, spontaneous polarization of carriers into a single symmetry-broken band with non-zero Chern number (and a consequent QAHE) has been predicted[6,7,35–37]. However, more exotic ground states with mixed spin and valley polarization may also be possible, and our experiment is not sensitive to the exact ground state polarization.

In addition to switching the magnetic ordering with $B_\perp$, we are able to control the magnetic state purely with charge doping at $B=0$. Figure 4d shows ρ_{yx} as the doping is swept back and forth, exhibiting opposite signs of the magnetic ordering for each sweep direction. By contrast, we do not observe switching on sweeping D back and forth (Fig. 4e). Doping-controlled switching of the magnetic order has recently been predicted due to the unique orbital magnetism exhibited in moiré vdW heterostructures[38]. However, in contrast to this prediction, our switching arises only within a few millitesla of $B=0$ (Extended Data Fig. 7) and thus probably originates from a different mechanism. Notably, the magnetic order does not switch precisely upon doping across $\nu=1$, but rather requires sweeping the doping far away from the magnetically ordered regime before returning. The switching occasionally occurs through metastable intermediate states and is observed more reliably when n is tuned slowly (Supplementary Fig. 5), suggesting that it is an intrinsic effect. Furthermore, the switching does not appear to depend on any other initialization conditions (Extended Data Fig. 8). Although we are not able to identify the valley and spin ordering of the surrounding symmetry-broken bands at $\nu=1$, this effect appears to be tied to a selective polarization of each of these bands with doping. The exact mechanism responsible for these unusual switching dynamics—including whether it is of a fundamental origin or related to sample inhomogeneity—remains an open question for future work.

The ability to electrically switch magnetic order is rare among known materials and can typically only be achieved with electric fields in multiferroics[39]. tMBG therefore provides a new platform for spintronics applications with purely doping-controlled magnetism and ultra-low power dissipation. More generally, our results demonstrate that the low symmetry of tMBG enables a wide array of highly tunable correlated states that differ on changing the sign of D. The addition of intrinsic non-trivial band topology also raises the possibility of realizing fractional Chern insulator states[40] in samples with stronger correlations at different twist angle or under pressure[3]. We anticipate that tMBG will be a crucial platform for further understanding these correlated and topological states of matter, providing unprecedented control with external tuning parameters.

Online content

Any methods, additional references, Nature Research reporting summaries, source data, extended data, supplementary information, acknowledgements, peer review information; details of author contributions and competing interests; and statements of data and code availability are available at https://doi.org/10.1038/s41567-020-01062-6.

Received: 25 June 2020; Accepted: 4 September 2020;

References

1. Cao, Y. et al. Correlated insulator behaviour at half-filling in magic-angle graphene superlattices. *Nature* **556**, 80–84 (2018).
2. Cao, Y. et al. Unconventional superconductivity in magic-angle graphene superlattices. *Nature* **556**, 43–50 (2018).
3. Yankowitz, M. et al. Tuning superconductivity in twisted bilayer graphene. *Science* **363**, 1059–1064 (2019).
4. Lu, X. et al. Superconductors, orbital magnets and correlated states in magic angle bilayer graphene. *Nature* **574**, 653–657 (2019).
5. Codecido, E. et al. Correlated insulating and superconducting states in twisted bilayer graphene below the magic angle. *Sci. Adv.* **5**, eaaw9770 (2019).
6. Sharpe, A. L. et al. Emergent ferromagnetism near three-quarters filling in twisted bilayer graphene. *Science* **365**, 605–608 (2019).
7. Serlin, M. et al. Intrinsic quantized anomalous Hall effect in a moiré heterostructure. *Science* **367**, 900–903 (2020).
8. Saito, Y., Ge, J., Watanabe, K., Taniguchi, T. & Young, A. F. Independent superconductors and correlated insulators in twisted bilayer graphene. *Nat. Phys.* **16**, 926–930 (2020).
9. Stepanov, P. et al. Untying the insulating and superconducting orders in magic-angle graphene. *Nature* **583**, 375–378 (2020).
10. Arora, H. S. et al. Superconductivity in metallic twisted bilayer graphene stabilized by WSe_2. *Nature* **583**, 379–384 (2020).
11. Burg, G. W. et al. Correlated insulating states in twisted double bilayer graphene. *Phys. Rev. Lett.* **123**, 197702 (2019).
12. Shen, C. et al. Correlated states in twisted double bilayer graphene. *Nat. Phys.* **16**, 520–525 (2020).
13. Cao, Y. et al. Tunable correlated states and spin-polarized phases in twisted bilayer-bilayer graphene. *Nature* **583**, 215–220 (2020).
14. Liu, X. et al. Tunable spin-polarized correlated states in twisted double bilayer graphene. *Nature* **583**, 221–225 (2020).
15. He, M. et al. Symmetry breaking in twisted double bilayer graphene. *Nat. Phys.* https://doi.org/10.1038/s41567-020-1030-6 (2020).
16. Chen, G. et al. Evidence of a gate-tunable Mott insulator in trilayer graphene moiré superlattice. *Nat. Phys.* **15**, 237–241 (2019).
17. Chen, G. et al. Signatures of tunable superconductivity in a trilayer graphene moiré superlattice. *Nature* **572**, 215–219 (2019).
18. Chen, G. et al. Tunable correlated Chern insulator and ferromagnetism in a moiré superlattice. *Nature* **579**, 56–61 (2020).
19. Tang, Y. et al. Simulation of Hubbard model physics in WSe_2/WS_2 moiré superlattices. *Nature* **579**, 353–358 (2020).
20. Regan, E. C. et al. Mott and generalized Wigner crystal states in WSe_2/WS_2 moiré superlattices. *Nature* **579**, 359–363 (2020).

21. Wang, L. et al. Correlated electronic phases in twisted bilayer transition metal dichalcogenides. *Nat. Mater.* **19**, 861–866 (2020).
22. Suárez Morell, E., Pacheco, M., Chico, L. & Brey, L. Electronic properties of twisted trilayer graphene. *Phys. Rev. B* **87**, 125414 (2013).
23. Ma, Z. et al. Topological flat bands in twisted trilayer graphene. Preprint at https://arxiv.org/pdf/1905.00622.pdf (2019).
24. Liu, J., Ma, Z., Gao, J. & Dai, X. Quantum valley Hall effect, orbital magnetism, and anomalous Hall effect in twisted multilayer graphene systems. *Phys. Rev. X* **9**, 031021 (2019).
25. Zondiner, U. et al. Cascade of phase transitions and Dirac revivals in magic-angle graphene. *Nature* **582**, 203–208 (2020).
26. Wong, D. et al. Cascade of electronic transitions in magic-angle twisted bilayer graphene. *Nature* **582**, 198–202 (2020).
27. Vignolles, D. et al. Field-induced spin-density wave in $(TMTSF)_2NO_3$. *Phys. Rev. B* **71**, 020404 (2005).
28. Rosenbaum, T., Field, S., Nelson, D. & Littlewood, P. Magnetic-field-induced localization transition in HgCdTe. *Phys. Rev. Lett.* **54**, 241–244 (1985).
29. Field, S., Reich, D. H., Rosenbaum, T., Littlewood, P. & Nelson, D. Electron correlation and disorder in $Hg_{1-x}Cd_xTe$ in a magnetic field. *Phys. Rev. B* **38**, 1856–1864 (1988).
30. Young, A. F. et al. Spin and valley quantum Hall ferromagnetism in graphene. *Nat. Phys.* **8**, 550–556 (2012).
31. Checkelsky, J. G., Li, L. & Ong, N. P. Divergent resistance at the Dirac point in graphene: evidence for a transition in a high magnetic field. *Phys. Rev. B* **79**, 115434 (2009).
32. Liu, X. et al. Tuning electron correlation in magic-angle twisted bilayer graphene using coulomb screening. Preprint at https://arxiv.org/pdf/2003.11072.pdf (2020).
33. Khalaf, E., Chatterjee, S., Bultinck, N., Zaletel, M. P. & Vishwanath, A. Charged skyrmions and topological origin of superconductivity in magic angle graphene. Preprint at https://arxiv.org/pdf/2004.00638.pdf (2020).
34. Kou, X. et al. Scale-invariant quantum anomalous hall effect in magnetic topological insulators beyond the two-dimensional limit. *Phys. Rev. Lett.* **113**, 137201 (2014).
35. Repellin, C., Dong, Z., Zhang, Y.-H. & Senthil, T. Ferromagnetism in narrow bands of moiré superlattices. *Phys. Rev. Lett.* **124**, 187601 (2020).
36. Bultinck, N., Chatterjee, S. & Zaletel, M. P. Mechanism for anomalous Hall ferromagnetism in twisted bilayer graphene. *Phys. Rev. Lett.* **124**, 166601 (2020).
37. Zhang, Y.-H., Mao, D. & Senthil, T. Twisted bilayer graphene aligned with hexagonal boron nitride: anomalous Hall effect and a lattice model. *Phys. Rev. Res.* **1**, 033126 (2019).
38. Zhu, J., Su, J.-J. & MacDonald, A. H. The curious magnetic properties of orbital Chern insulators. Preprint at https://arxiv.org/pdf/2001.05084.pdf (2020).
39. Matsukura, F., Yokura, Y. & Ohno, H. Control of magnetism by electric fields. *Nat. Nanotechnol.* **10**, 209–220 (2015).
40. Zhang, Y.-H., Mao, D., Cao, Y., Jarillo-Herrero, P. & Senthil, T. Nearly flat Chern bands in moiré superlattices. *Phys. Rev. B* **99**, 075127 (2019).

Methods

Device fabrication. The tMBG devices were fabricated using the 'cut-and-stack' method[8]. We identified exfoliated graphene flakes with regions of both monolayer and bilayer graphene, then used an atomic force microscope (AFM) tip to isolate a region from each area[8,16]. We found that, in general, longer AFM-cut edges can increase the friction between rotated graphene sheets and improve the yield of devices near the targeted twist angle. Samples were assembled using a standard dry transfer technique that utilized a polycarbonate film on top of a polydimethylsiloxane dome[41]. Completed heterostructures were transferred onto a Si/SiO$_2$ wafer. The temperature was kept below 180 °C during device fabrication to preserve the intended twist angle. All devices were encapsulated between flakes of BN with a typical thickness of 30–40 nm and had graphite top and bottom gates (except the device with a twist angle of 1.44°, which had a silicon bottom gate). In devices with a graphite bottom gate, a gate voltage was applied to the Si gate to dope the region of the graphene contacts overhanging the graphite back gate to a high charge carrier density and to reduce the contact resistance.

Transport measurements. We measured the electrical transport in four tMBG devices with twist angles varying between $\theta = 0.89°$ and 1.55° (Extended Data Figs. 1, 2 and 9). Many of the salient transport features observed at each twist angle were qualitatively similar to those observed in devices at slightly different twist angles (for a comparison see Fig. 4a and Extended Data Fig. 2). Transport measurements were conducted in a four-terminal geometry with a.c. current excitation of 10–20 nA using standard lock-in techniques at either 13.3 Hz or 17.7 Hz. The magnetic hysteresis loops in device D2 were measured using a 500 pA excitation. A d.c. current bias, I_{dc}, could also be added to further control the magnetic state (Supplementary Fig. 6), as discussed previously for devices of tBLG aligned with BN[6,7]. n and D could be tuned by the gate voltages through the relation $n = (C_{TG}V_{TG} + C_{BG}V_{BG})/e$, $D = |(C_{TG}V_{TG} - C_{BG}V_{BG})/2|$, where C_{TG} and C_{BG} are, respectively, the capacitances between the top (TG) and bottom (BG) gates and the tMBG, and e is the electron charge. We chose a convention such that $D > 0$ corresponds to the field pointing from the monolayer to bilayer graphene.

Twist angle determination. The twist angle θ was determined from the values of charge carrier density at which the insulating states at $\nu = \pm 4 = \pm n_s$ were observed, following $n_s = 8\theta^2/\sqrt{3}a^2$, where $a = 0.246$ nm is the lattice constant of graphene. The values of $\pm n_s$ were determined from the sequence of quantum oscillations in a magnetic field that project to $\pm n_s$ (or $\pm n_s/2$ for $\theta = 1.08°$; Extended Data Fig. 10).

Band structure calculation. We calculated the band structure using the standard continuum model. The Hamiltonian is

$$H = H_{\mathrm{MG}} + H_{\mathrm{BG}} + H_{\mathrm{M}}$$

where H_{MG} and H_{BG} are the Hamiltonians for the monolayer graphene and the bilayer graphene, respectively. H_{M} is the coupling term between the monolayer and bilayer graphene. We have

$$H_{\mathrm{MG}} = \sum\nolimits_{\mathbf{k}} \left(\tilde{c}^{\dagger}_{\mathrm{A}}(\mathbf{k}), \tilde{c}^{\dagger}_{\mathrm{B}}(\mathbf{k})\right) \begin{pmatrix} M - \frac{\delta}{2} & -\frac{\sqrt{3}}{2}t(\tilde{k}_x - i\tilde{k}_y) \\ -\frac{\sqrt{3}}{2}t(\tilde{k}_x + i\tilde{k}_y) & -M - \frac{\delta}{2} \end{pmatrix} \begin{pmatrix} \tilde{c}_{\mathrm{A}}(\mathbf{k}) \\ \tilde{c}_{\mathrm{B}}(\mathbf{k}) \end{pmatrix}$$

where $\tilde{\mathbf{k}} = R(-\theta/2)\mathbf{k}$, with θ being the twist angle. $R(\varphi)$ is the transformation matrix for anticlockwise rotation with angle φ.

The Hamiltonian for the bilayer graphene is

$$H_{\mathrm{BG}} = \sum\nolimits_{\mathbf{k}} \Psi^{\dagger}(\mathbf{k}) \begin{pmatrix} 0 & -\frac{\sqrt{3}}{2}t(\tilde{k}_x - i\tilde{k}_y) & -\frac{\sqrt{3}}{2}\gamma_4(\tilde{k}_x - i\tilde{k}_y) & -\frac{\sqrt{3}}{2}\gamma_3(\tilde{k}_x + i\tilde{k}_y) \\ -\frac{\sqrt{3}}{2}t(\tilde{k}_x + i\tilde{k}_y) & 0 & \gamma_1 & -\frac{\sqrt{3}}{2}\gamma_4(\tilde{k}_x - i\tilde{k}_y) \\ -\frac{\sqrt{3}}{2}\gamma_4(\tilde{k}_x + i\tilde{k}_y) & \gamma_1 & -\frac{\delta}{2} & -\frac{\sqrt{3}}{2}t(\tilde{k}_x - i\tilde{k}_y) \\ -\frac{\sqrt{3}}{2}\gamma_3(\tilde{k}_x - i\tilde{k}_y) & -\frac{\sqrt{3}}{2}\gamma_4(\tilde{k}_x + i\tilde{k}_y) & -\frac{\sqrt{3}}{2}t(\tilde{k}_x + i\tilde{k}_y) & \frac{\delta}{2} \end{pmatrix} \Psi(\mathbf{k})$$

where $\tilde{\mathbf{k}} = R(\theta/2)\mathbf{k}$ and $\Psi^{\dagger}(\mathbf{k}) = \left(c^{\dagger}_{\mathrm{A}_1}(\mathbf{k}), c^{\dagger}_{\mathrm{B}_1}(\mathbf{k}), c^{\dagger}_{\mathrm{A}_2}(\mathbf{k}), c^{\dagger}_{\mathrm{B}_2}(\mathbf{k})\right)$.

Finally, the interlayer moiré tunnelling term is

$$H_{\mathrm{M}} = \sum\nolimits_{\mathbf{k}} \sum\nolimits_{j=0,1,2} \left(\tilde{c}^{\dagger}_{\mathrm{A}}(\mathbf{k}), \tilde{c}^{\dagger}_{\mathrm{B}}(\mathbf{k})\right) \begin{pmatrix} \alpha t_{\mathrm{M}} & t_{\mathrm{M}} e^{-i\frac{2\pi}{3}j} \\ t_{\mathrm{M}} e^{i\frac{2\pi}{3}j} & \alpha t_{\mathrm{M}} \end{pmatrix} \begin{pmatrix} c_{\mathrm{A}_1}(\mathbf{k} + \mathbf{Q}_j) \\ c_{\mathrm{B}_1}(\mathbf{k} + \mathbf{Q}_j) \end{pmatrix} + \mathrm{h.c.}$$

where $\mathbf{Q}_0 = (0, 0)$, $\mathbf{Q}_1 = \frac{1}{a_{\mathrm{M}}}\left(-\frac{2\pi}{\sqrt{3}}, -2\pi\right)$ and $\mathbf{Q}_2 = \frac{1}{a_{\mathrm{M}}}\left(\frac{2\pi}{\sqrt{3}}, -2\pi\right)$, with a_{M} being the moiré lattice constant.

Here $\tilde{c}_{\alpha}(\mathbf{k})$ and $c_{\alpha}(\mathbf{k})$ are electron operators for the monolayer graphene and bilayer graphene, respectively. We take parameters $(t, \gamma_1, \gamma_3, \gamma_4) = (-2{,}610, 361, 283, 140)$ meV. For the interlayer tunnelling, we take $t_{\mathrm{M}} = 110$ meV and $\alpha = 0.5$. M is a sublattice potential term for the monolayer graphene that may originate from hBN alignment. We use $M = 10$ meV. δ is the potential difference, which is tuned by the displacement field D.

With sufficient $|\delta|$, the neutrality gap is opened and we can define the valley Chern number for the conduction and valence bands. Here we focus on the conduction band, and at $\theta = 1.08°$ the valley Chern number is $|C| = 2$ and $|C| = 1$ for the $D > 0$ and $D < 0$ sides, respectively.

Data availability

All data that support the plots within this paper and other findings of this study are available from the corresponding author upon reasonable request. Source data are provided with this paper.

References

41. Wang, L. et al. One-dimensional electrical contact to a two-dimensional material. *Science* **342**, 614–617 (2013).

Acknowledgements

We thank A. Young, H. Polshyn, A. Millis, C.-Z. Chang, J.-H. Chu and E. Khalaf for helpful discussions. The research on correlated states in twisted monolayer–bilayer graphene was primarily supported as part of Programmable Quantum Materials, an Energy Frontier Research Center funded by the US Department of Energy (DOE), Office of Science, Basic Energy Sciences (BES), under award DE-SC0019443. The measurements and understanding of ferromagnetism at the University of Washington were partially supported by NSF MRSEC 1719797. M.Y. is an Army Research Office Young Investigator (W911NF-20-1-0211). X.X. acknowledges support from the Boeing Distinguished Professorship in Physics. X.X. and M.Y. acknowledge support from the State of Washington funded Clean Energy Institute. This work made use of a dilution refrigerator system provided by NSF DMR-1725221. K.W. and T.T. acknowledge support from the Elemental Strategy Initiative conducted by the MEXT, Japan (grant no. JPMXP0112101001), JSPS KAKENHI (grant no. JP20H00354) and CREST (JPMJCR15F3), JST.

Author contributions

S.C., M.H. and V.H. fabricated the devices and performed the measurements. Y.-H.Z. performed the calculations. Z.F. and D.H.C. assisted with measurements in the dilution refrigerator. K.W. and T.T. grew the BN crystals. S.C., M.H., X.X., C.R.D. and M.Y. analysed the data and wrote the manuscript with input from all authors.

Competing interests

The authors declare no competing interests.

Additional information

Extended data is available for this paper at https://doi.org/10.1038/s41567-020-01062-6.

Supplementary information is available for this paper at https://doi.org/10.1038/s41567-020-01062-6.

Correspondence and requests for materials should be addressed to X.X., C.R.D. or M.Y.

Reprints and permissions information is available at www.nature.com/reprints.

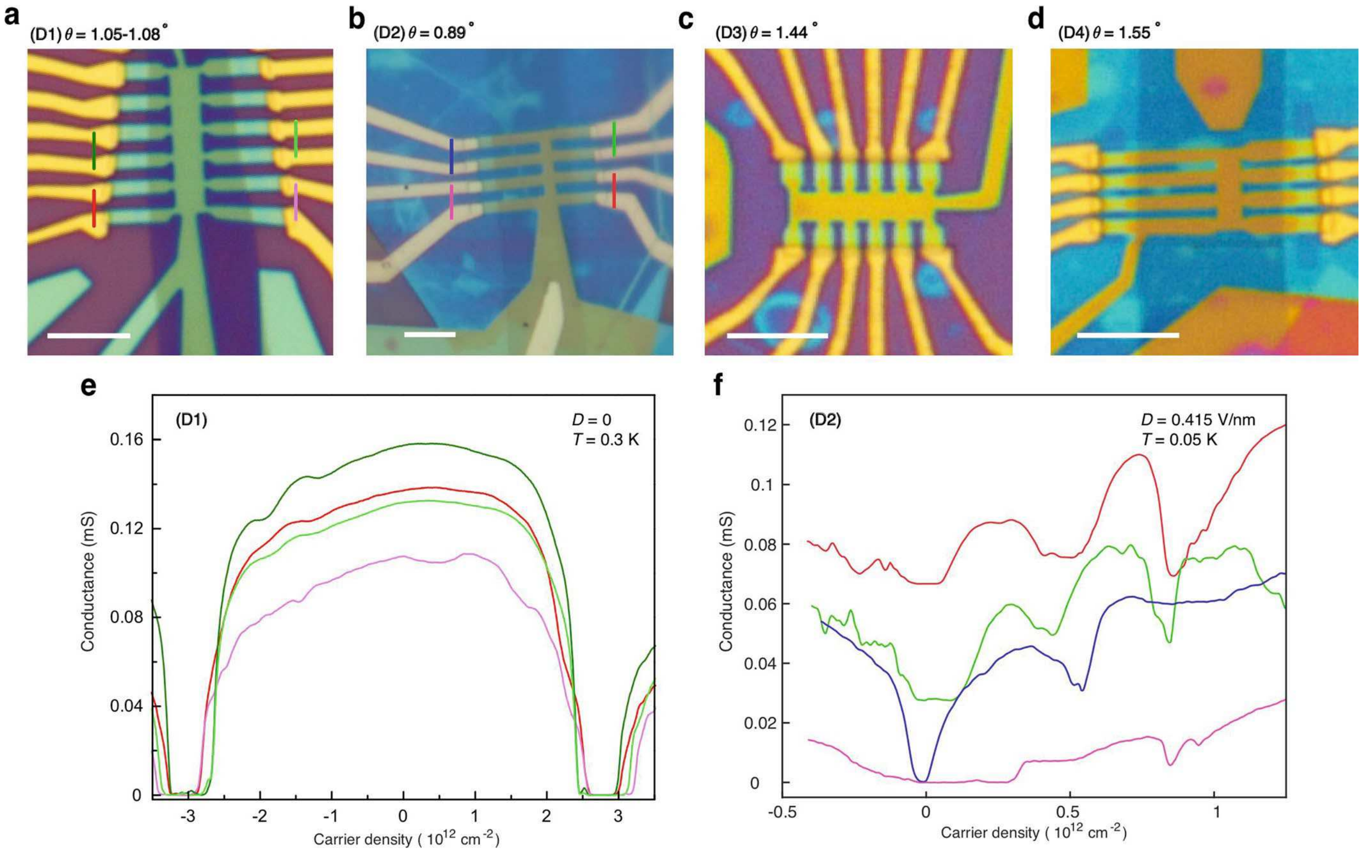

Extended Data Fig. 1 | Optical microscope images and two-terminal conductance of the tMBG devices. (**a-d**), the twist angle of each device is denoted at the bottom left corner of each image. All scale bars are 5 μm. (**e-f**) show the two-terminal conductance measured between neighbouring pairs of contacts as indicated by the colour-coded bars in (**a-b**). Device D1 exhibits a small twist angle gradient of approximately 0.03° primarily along the longitudinal direction of the Hall bar. Device D2 exhibits a larger twist angle inhomogeneity of approximately 0.1°, consistent with the apparent doubling of some of the transport features in Fig. 4a of the main text.

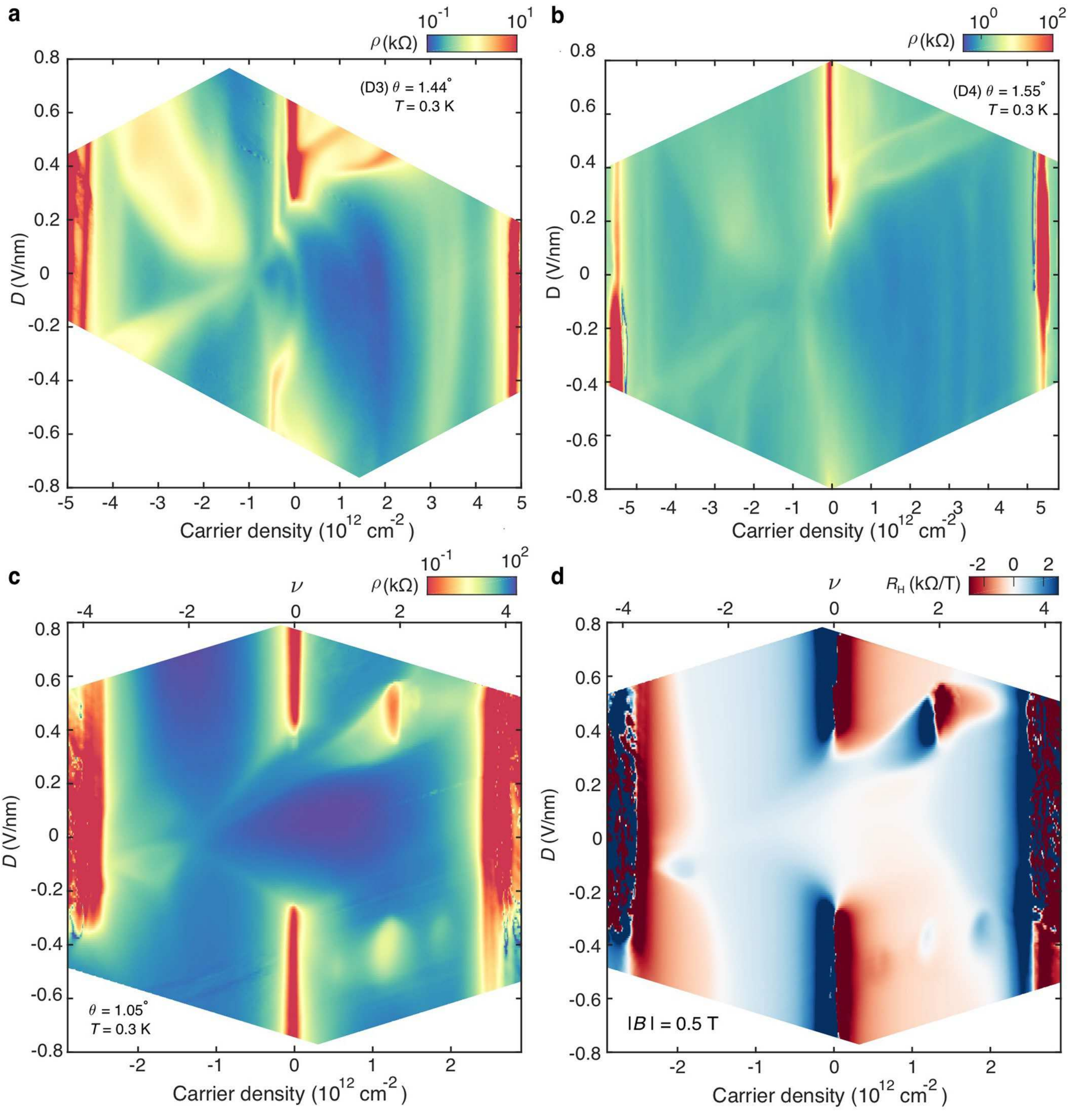

Extended Data Fig. 2 | Transport in tMBG at a variety of twist angles at T = 300 mK. ρ as a function of n and D for (**a**) device D3 (θ = 1.44°), and (**b**) device D4 (θ = 1.55°). At these twist angles, the gap at the charge neutrality points only opens for $D > 0$ (pointing from monolayer to bilayer graphene). Features corresponding to single particle vHs can be seen in both conduction and valence bands. Although some features may arise owing to correlations, we do not observe any states with insulating behavior at integer ν within the bands. **c-d**, ρ and R_H for device D1 using different contacts from Fig. 1d-e of the main text. The twist angle, θ = 1.05°, is slightly smaller than for the region of the device probed in the main text.

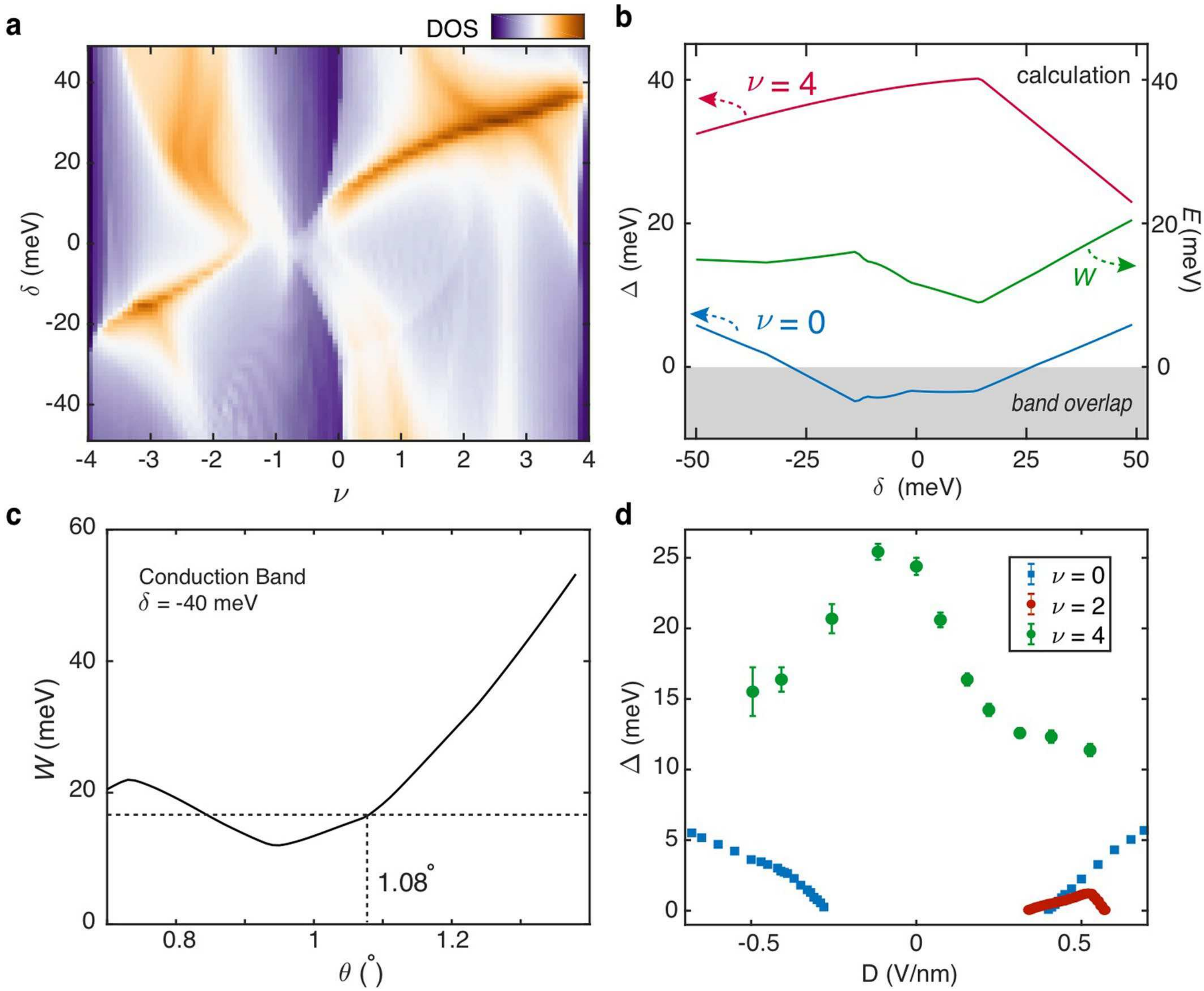

Extended Data Fig. 3 | Energy scales and density of states of tMBG. a, Single-particle density of states (DOS) calculated for $\theta = 1.08°$ as a function of ν and D, following the model described in the text. **b**, Calculated single particle gaps at $\nu = 0, +4$ (left axis) as a function of interlayer potential, δ. Bandwidth of the conduction band, W (right axis). The bandwidth does not vary widely over our this range of δ. **c**, W calculated as function of θ for $\delta = -40$ meV. W does not change substantially for $0.85^\circ < \theta < 1.1^\circ$. **d**, Experimentally measured energy gaps of $\nu = 0, +2, +4$ as a function of D in device D1 ($\theta = 1.08^\circ$). The single particle gaps at $\nu = 0, +4$ are qualitatively consistent with the predictions in **b**. A CI gap at $\nu = +2$ only emerges over a finite range of $D > 0$.

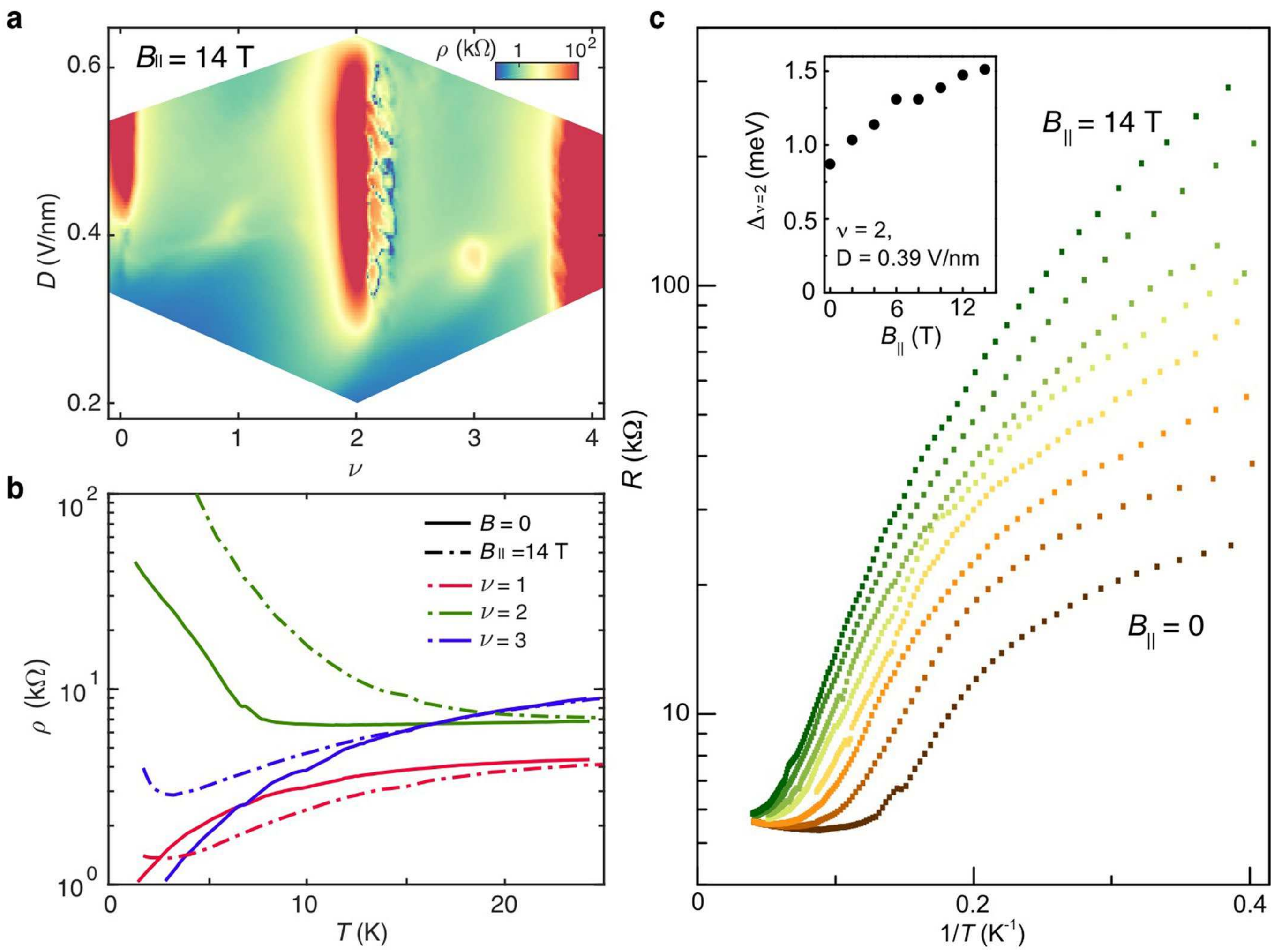

Extended Data Fig. 4 | Transport in an in-plane magnetic field in device D1. **a**, ρ as a function of ν and D at $B_{\parallel} = 14$ T. **b**, $\rho(T)$ for $\nu = 1, 2, 3$ at both $B = 0$ (solid curves) and $B_{\parallel} = 14$ T (dashed curves). In the former, $\nu = 2$ exhibits insulating behavior whereas $\nu = 1$ and 3 are metallic. In the latter, all become more resistive at low temperature, and $\nu = 1$ and 3 begin to undergo an insulating transition at low temperature. **c**, Device resistance, R, versus T^{-1} at $\nu = 2$ and $D = +0.39$ V/nm. (Inset) Energy gaps, $\Delta_{\nu=2}$, as function of $B_{\parallel}$, extracted from the thermal activation measurements. Gaps are extracted by fitting the data in the main panel to $R \propto e^{\Delta/2k_BT}$, where k_B is the Boltzmann constant. The gap grows with larger $B_{\parallel}$ suggestive of a spin-polarized ground state. However, thermal activation measurements may be complicated by additional orbital contributions owing to the multilayer structure of tMBG[15].

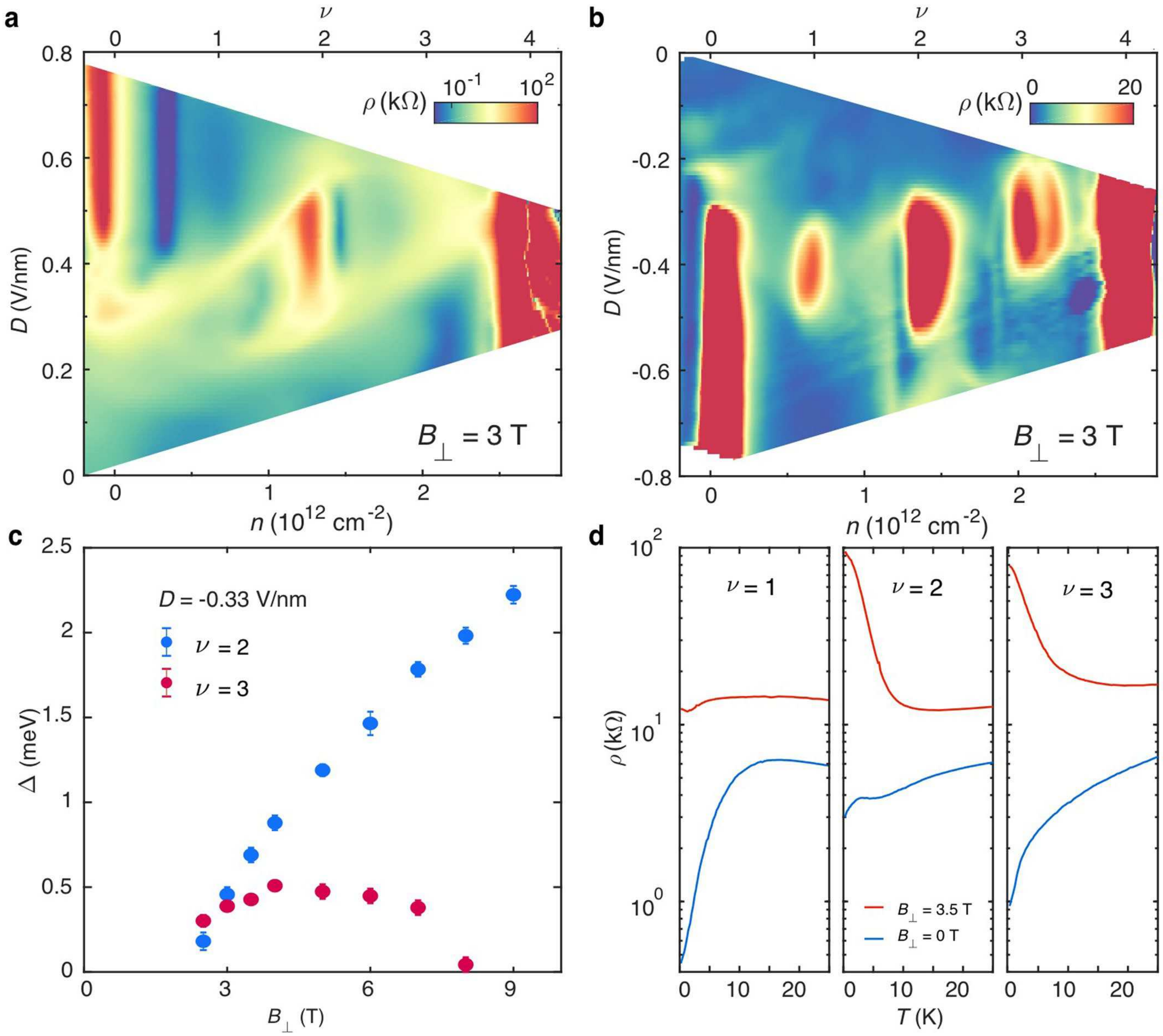

Extended Data Fig. 5 | High magnetic field transport in device D1. a, ρ as a function of n and D for $D > 0$ at $B_\perp = 3$ T. In addition to the CI state at $\nu = 2$, vertical blue stripes correspond to the formation of Landau levels within the symmetry broken halo region. **b**, ρ for $D < 0$ at $B_\perp = 3$ T. Field-assisted CI states emerge over a finite range of D, along with associated quantum oscillations. **c**, Energy gaps of $\nu = 2$ and 3 at $D = -0.33$ V/nm as a function of $B_\perp$, measured by thermal activation. The gap at $\nu = 3$ closes at high field, which may be related to the spin and valley ordering of the state, and/or competition with Landau level formation. **d**, $\rho(T)$ corresponding to $\nu = 1, 2, 3$ at $B_\perp = 0$ and 3.5 T. All exhibit unusual metallic temperature dependence at $B = 0$, but are insulating ($\nu = 2, 3$) or near a crossover point ($\nu = 1$) at high field.

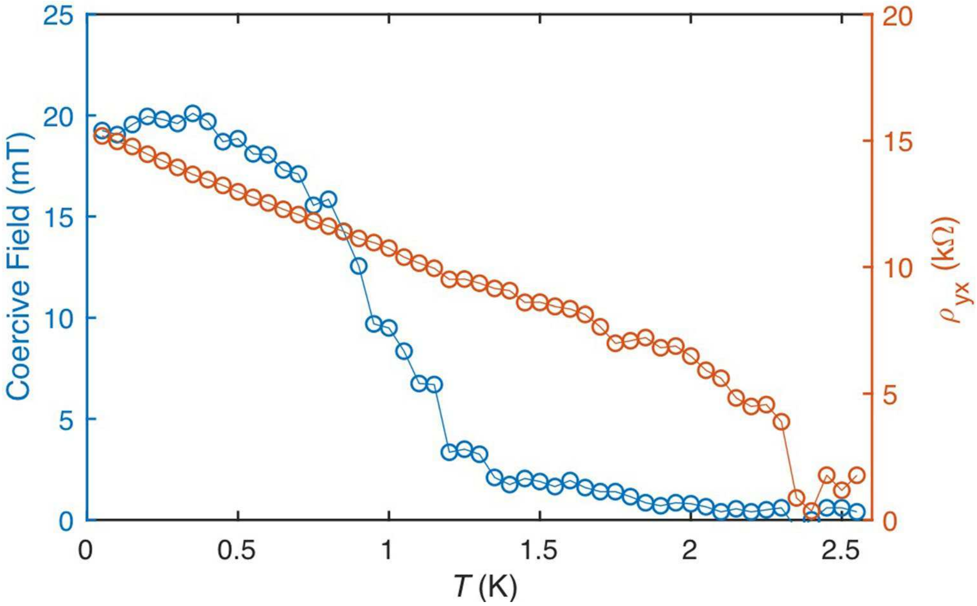

Extended Data Fig. 6 | Temperature dependence of the AHE resistivity and coercive field in device D2. Measurements correspond to the data set shown in Fig. 4b of the main text, with $\nu = 0.94$ and $D = +\,0.415$ V/nm.

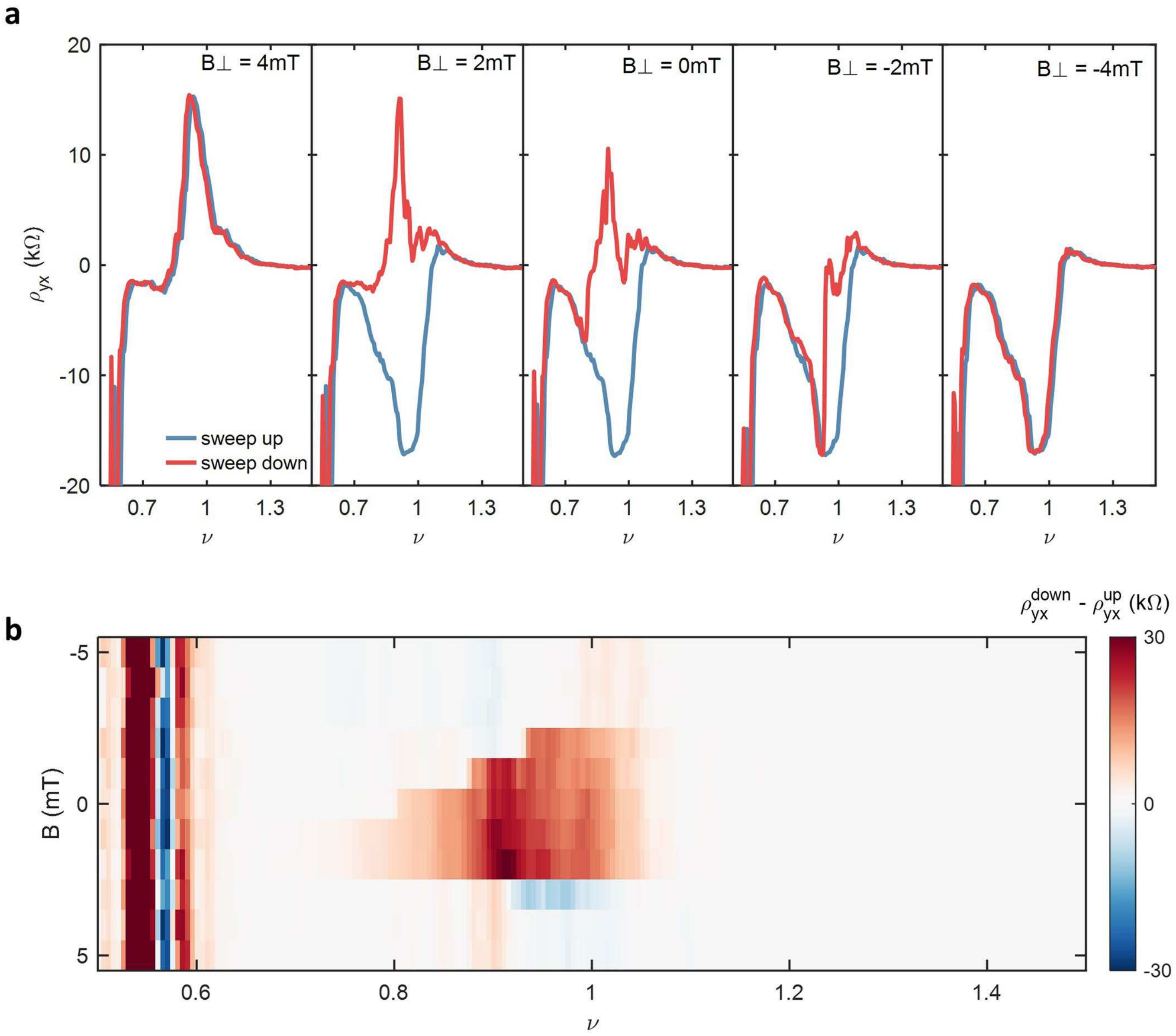

Extended Data Fig. 7 | Doping-induced switching of the magnetic order with $B_\perp$ in device D2. a, ρ_{yx} as ν is swept back and forth from -0.5 to +2.5 at $D = +0.415$ V/nm, with $B_\perp = +4$ mT, +2mT, 0mT, − 2 mT, − 4 mT. Doping-induced switching of the magnetic order is only observed within a small range of $B_\perp$ from ~ + 2 mT to − 2 mT. At larger $B_\perp$, the magnetic state is aligned with the applied field regardless of the sweep direction. The measurement is performed subsequent to thermally-cycling the device to $T = 4$ K — above the Curie temperature — and then back to base temperature. **b**, The difference between ρ_{yx} sweeping up and down as a function of $B_\perp$. The red region denotes the regime in which the magnetization can be switched with doping.

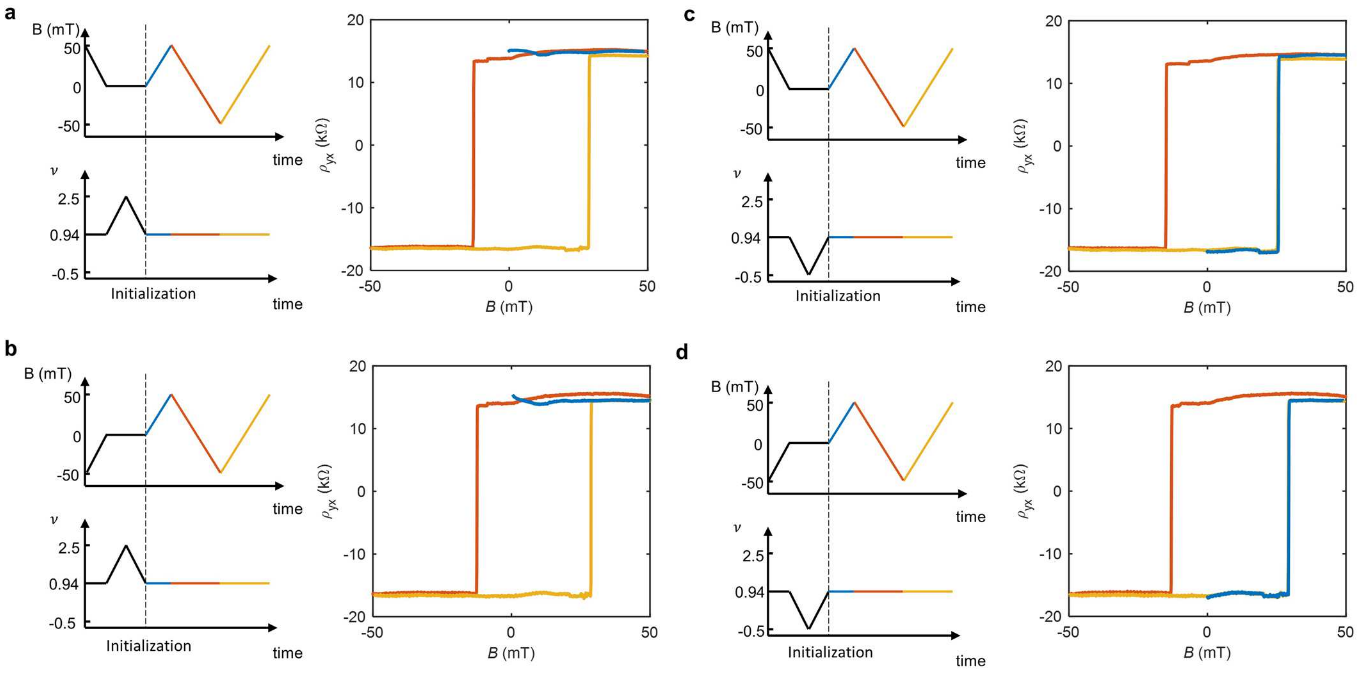

Extended Data Fig. 8 | Dependence of doping-induced switching on magnetic field initialization in device D2. a-d, show hysteresis loops at $\nu = 0.94$ and $D = +\ 0.415$ V/nm, acquired after initiating the state with different magnetic field and doping trainings. The schematics to the left of each ρ_{yx} panel denote the sequence of $B_{\perp}$ and ν sweeps as a function of time. Black lines denote the initialization operations, performed prior to data acquisition. The initialized magnetic state is indicated by the starting point of the blue ρ_{yx} curve at $B = 0$. Subsequent to the initialization, ν is held fixed at 0.94 while $B_{\perp}$ is swept back and forth. Notably, independent of the field training history, ρ_{yx} is initialized to the positive state when ν is swept down from 2.5, and to the negative state when ν is swept up from $-$ 0.5. Subsequent magnetic field sweeping forms a similar hysteresis loop independent of the initialized state. This helps to rule out any effects of the magnetic field initialization in our observations of the doping-induced switching effect at $B = 0$.

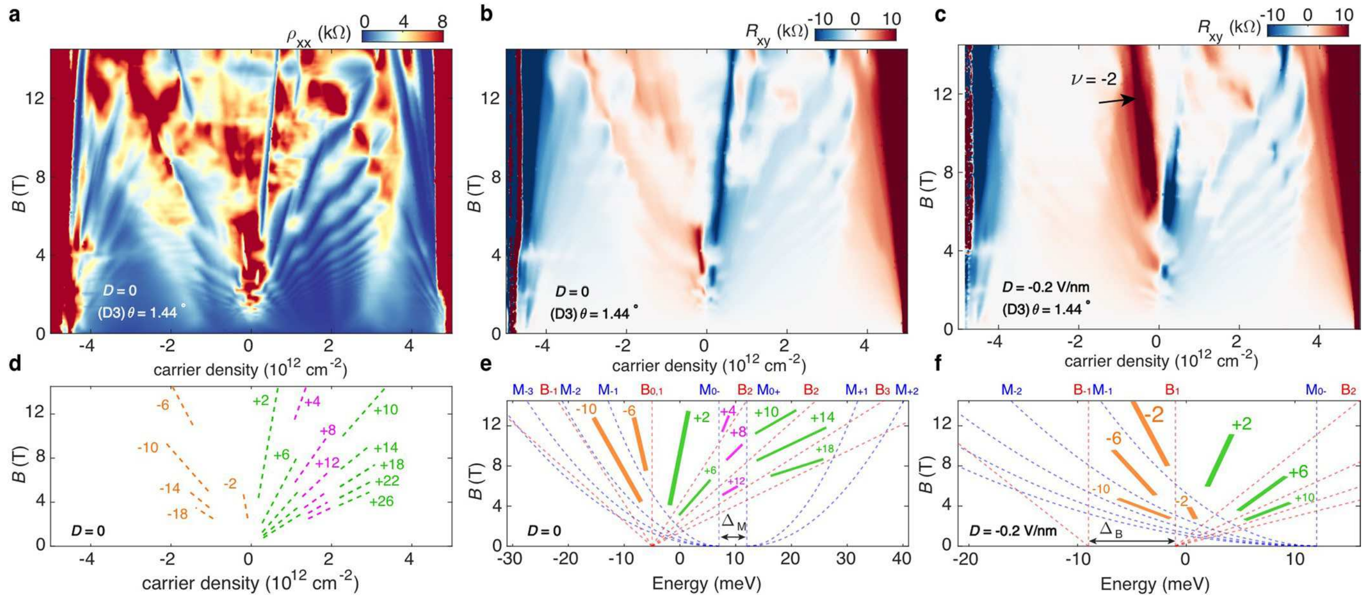

Extended Data Fig. 9 | Quantum oscillations in device D3 ($\theta = 1.44°$). **a**, ρ_{xx} and **b**, R_{xy} as a function of n and $B_\perp$ at $D = 0$. **c**, Comparable R_{xy} map at $D = -0.2$ V/nm. **d**, Schematic illustration of the prominent quantum oscillations observed in **a**. Quantum oscillations exhibit four-fold degeneracy at each value of n. For $n < 0$, we observe a sequence of quantum oscillations with filling factors $\nu_{LL} = -2, -6, -10....$ For $n > 0$, the sequence shifts from $+2, +6, +10...$ to $+4, +8, +12, ...$ and back again as n is raised. These sequences can be understood by considering the monolayer- and bilayer-like corners of the moiré Brillouin zone as approximately uncoupled owing to the larger twist angle, in which the dominant quantum oscillations are the sum of the contributions from each band. **e**, Dashed blue lines denote the Landau levels of the monolayer-like bands as a function of energy, following $E_{LL,m} = \sqrt{2e\hbar v_F^2 NB}$, where N is the Landau level index and v_F is the Fermi velocity. Dashed red lines denote the same for the bilayer-like bands, with $E_{LL,b} = \frac{e\hbar B}{m^*}\sqrt{N(N-1)}$, where m^* is the effective mass. The total filling factor ν_{LL} within each gap is given by the sum of the Landau level indexes for each band (solid bars). The experimentally observed sequence of quantum oscillations is well reproduced taking $v_F = 1.44 \times 10^5$ m/s, $m^* = 0.14m_0$, and including a charge neutrality band gap in the monolayer spectrum of $\Delta_M = 5$ meV and an offset between the monolayer and bilayer charge neutrality points of $\delta = 14.5$ meV (indicative of band overlap). **f**, Similar energy diagram for $D = -0.2$ V/nm. To account for the observation of $\nu_{LL} = -2$ at high magnetic field, a band gap for the bilayer spectrum of $\Delta_B = 8$ meV is included, and we take $\delta = 19.5$ meV.

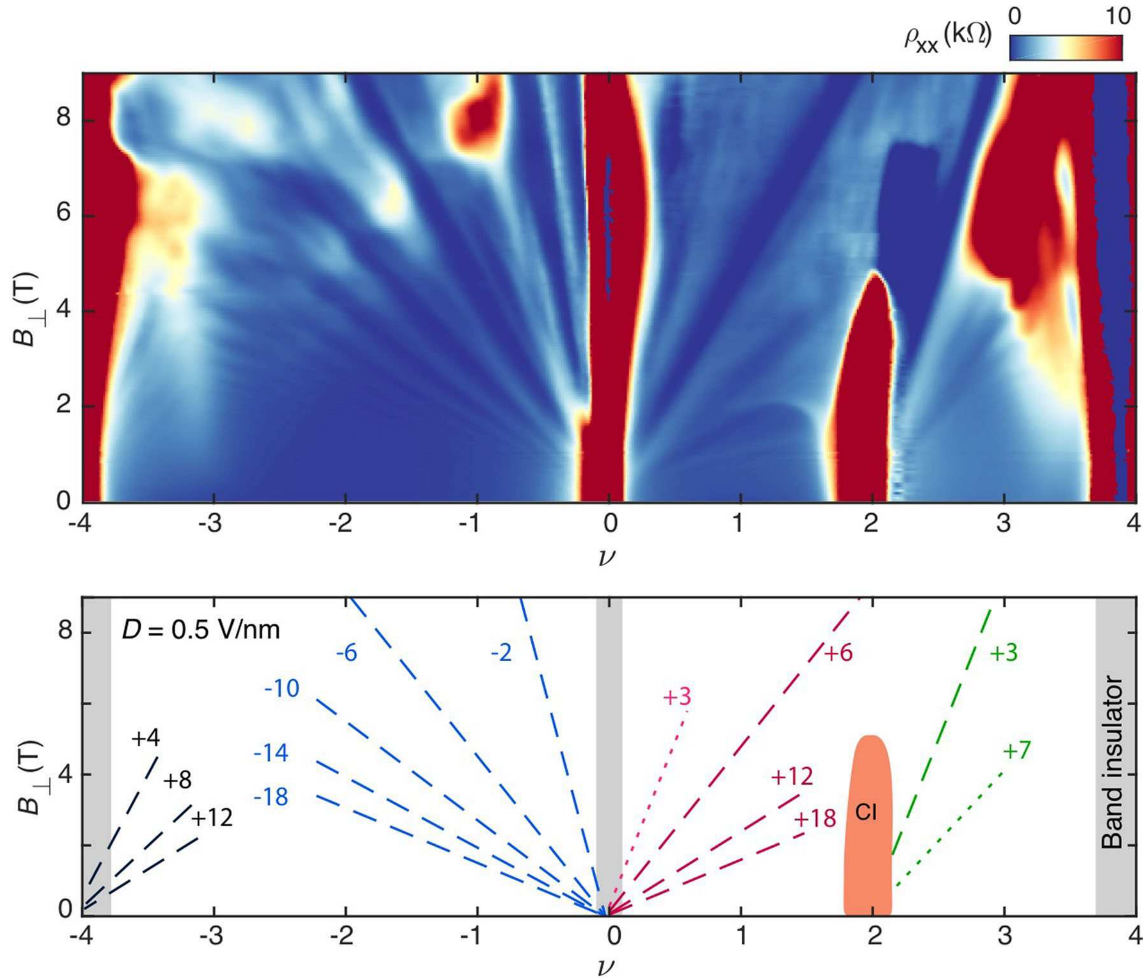

Extended Data Fig. 10 | Quantum oscillations at $D = +0.5$ V/nm in device D1 ($\theta = 1.08°$). Landau fan diagram up to full filling of the moiré unit cell with $D = +0.5$ V/nm at $T = 300$ mK. Separate sequences of quantum oscillations emerge from $\nu = -4$ with a dominant sequence of $\nu_{LL} = +4, +8, +12, \ldots$, from $\nu = 0$ with dominant sequences of $\nu_{LL} = -2, -6, -10, \ldots$ and $\nu_{LL} = +6, +12, +18, \ldots$, and from $\nu = +2$ with a dominant state at $\nu_{LL} = +3$. Quantum oscillations emerging from $\nu = +2$ with larger filling factor do not follow a simple sequence, which may be a consequence of structural disorder in the sample. These states are illustrated schematically in the bottom panel with dashed lines. Dotted lines show additional states which emerge at higher field. Gray shaded regions denote band insulators and the orange shaded region denotes the CI state. The apparent 6-fold degeneracy of electron-like quantum oscillations emerging from $\nu = 0$ may indicate the presence of multiple Fermi surface pockets within the moiré Brillouin zone.